Retrieval of sea surface wind speed from spaceborne SAR over the Arctic marginal ice zone with a neural network

Xiao-Ming Li, *Member, IEEE*, Tingting Qin and Ke Wu

***Abstract*—In this paper, we presented a method of retrieving sea surface wind speed from Sentinel-1 synthetic aperture radar (SAR) horizontal-horizontal (HH) polarization data in extra-wide mode, which have been extensively acquired over the Arctic for sea ice monitoring. In contrast to the conventional algorithm, i.e., using a geophysical model function (GMF) to retrieve sea surface wind by spaceborne SAR, we introduced an alternative method based on physical model guided neural network. Parameters of SAR normalized radar cross section, incidence angle, and wind direction are used as the inputs of the backward propagation (BP) neural network, and the output is the sea surface wind speed. The network is developed based on more than 11,000 HH-polarized EW images acquired in the marginal ice zone (MIZ) of the Arctic and their collocations with scatterometer measurements. Verification of the neural network based on the testing dataset yields a bias of 0.23 m/s and a root mean square error (RMSE) of 1.25 m/s compared to the scatterometer wind speed. Further comparison of the SAR retrieved sea surface wind speed with independent buoy measurements shows a bias and RMSE of 0.12 m/s and 1.42 m/s, respectively. We also analyzed the uncertainty of retrieval when the wind direction data of a reanalysis model are used as inputs to the neural network. By combining the detected sea ice cover information based on the EW data, one can expect to derive simultaneously sea ice and marine-meteorological parameters by spaceborne SAR in a high spatial resolution in the Arctic.**

***Index Terms*—Synthetic Aperture Radar, sea surface wind, machine learning**

I. Introduction

Retrieval of sea surface wind (SSW) by spaceborne synthetic aperture radar (SAR) has been studied for a few decades. The general retrieval method adopts the geophysical model function (GMF), which was designed for a microwave scatterometer to retrieve SSW field. The GMFs generally have the following format:

$$\sigma_0 = a_0(\theta, u_{10})[1 + a_1(\theta, u_{10})\cos\phi + a_2(\theta, u_{10})\cos 2\phi]^p \quad (1)$$

The GMF empirically relates the normalized radar cross section (NRCS, σ_0) with SSW speed u_{10}, azimuthal wind direction ϕ and incidence angle θ through various linear or nonlinear functions of a_0, a_1 and a_2. Different GMFs for C-band radar data with vertical-vertical (VV) polarization have been proposed and are widely exploited to acquire SSW at a high spatial resolution, e.g., from CMOD4, CMOD5, and CMOD5.N to the currently used CMOD7 [1] - [5], and CMOD_IFR2 [6]. On the other hand, as spaceborne SAR can also operate in horizontal-horizontal (HH) polarization, the so-called polarization ratio (PR) should be used to transform the NRCS of HH-polarization to that of VV polarization and then the GMFs developed for VV polarization data can be applied to retrieve the SSW speed. However, the dependence of PR is not only on incidence angle [7] - [9] but also on SSW conditions [8],[10]. While PR depends on various factors, one can also develop independent GMFs for HH-polarized spaceborne SAR data, e.g., as proposed by Monaldo *et al.* [11] for the Radarsat data and by Zhang *et al.* [12] for ENVISAT/ASAR data in HH polarization. This should be an optimized method to retrieve SSW by spaceborne SAR in HH polarization, as the PR may depend on various factors through nonlinear relations.

When spaceborne SAR operating in different microwave frequencies from C-band are in orbit, the functions in (1) must be refit to make them suitable for retrieving SSW, e.g., the LMOD [13] for the L-band ALOS/PALSAR and the XMOD [14] for the X-band TerraSAR-X and TanDEM-X. Although the format of (1) is compact, the functions a_0, a_1 and a_2 are complicated; they often consist of sub-functions and generally, more than 30 coefficients need to be determined. Moreover, to our knowledge, the formats of these functions are empirically fitted to a large amount of tuning data.

Both Sentinel-1A (S1A) and Sentinel-1B(S1B) have been in orbit since June 2016 and have acquired extensive the extra-wide (EW) swath data with a polarization combination of HH and horizontal-vertical (HV) for sea ice monitoring in the Arctic. The marginal ice zone (MIZ) is generally defined as the transit area of sea ice and open water, where the sea ice concentration is between 15% and 80%. Along with the rapid decline of sea ice in the Arctic, its seasonal MIZ is widening [15], which leads to significant interaction between sea ice and ocean dynamics. Therefore, we intend to derive SSW at high spatial resolution from these EW data acquired in the Arctic, in combination with sea ice information for supporting scientific research, resource utilization and navigation safety.

We preliminarily analyzed the combinations of CMOD5.N and different PR models for retrieving sea surface wind speed by the S1 HH-polarized data [16] acquired over MIZ of the Arctic.

The manuscript was submitted on May 10, 2020

This work was supported in part National Key Research and Development Project (2018YFC1407100) China. (Corresponding author: Xiao-Ming Li.)

All the authors are with the Key Laboratory of Digital Earth, Aerospace Information Research Institution, Chinese Academy of Sciences, Beijing, 100094, P. R. China (e-mail: lixm@radi.ac.cn).

Preprints (www.preprints.org) | NOT PEER-REVIEWED | Posted: 18 May 2020 doi:10.20944/preprints202005.0300.v1

The comparisons suggest that the PR models developed in [8] and [10] have better performances on retrieving SSW speed. Machine learning algorithms have demonstrated their great potential for mining information from ocean remote sensing imagery (e.g., as reviewed in [17]), and they generally have a strong capability of fitting the nonlinear curves, e.g., the one depicted by (1). As described before, tuning the GMFs for spaceborne SAR data is a challenge because there are multiple non-linear functions and sub-functions that need to be empirically or statistically determined. Therefore, in this paper, we present a method of retrieving SSW from S1 EW data in HH-polarization based on a neural network.

Following the introduction, the methodology including the datasets and the construction of a backward propagation (BP) neural network, are described in Section II. We verified the trained BP neural network by comparing retrieval with the advanced scatterometer (ASCAT) data. Then we further validated the retrieval by comparing it with in situ buoy measurements and the measurements from the Chinese icebreaker "XueLong" in the Arctic. These comparisons are presented in Section III. A summary and conclusions are given in the last section.

II. Methodology

A. S1 data and their collocations with ASCAT data

Both S1A and S1B EW mode data with a swath width of 400 km in HH polarization are used in this study. The incidence angle of the EW data varies between 19° and 47°. Radiometric calibration and thermal noise removal of the EW data is conducted according to the S1 user manual [18]; referring to the appendix for details.

The daily EUMETSAT ASCAT-A/B SSW data under all weather conditions with a spatial resolution of 0.25° by 0.25° were collected in this study. The S1 EW data were spatially and temporally collocated with ASCAT wind data with a spatial distance of less than 25 km and a temporal window of less than 60 minutes, respectively, which yields a total of 11, 431 scenes of S1 EW imagery, among which 8,452 and 2,979 scenes were acquired by S1A and S1B, respectively, collocated with ASCAT measurements over the Arctic MIZ from 2015 to 2018. The spatial distribution of these collocations is shown in Fig.1. The majority of the collocations are in the Atlantic sector of the Arctic.

The unavoidable existence of speckles in SAR image makes it impossible to retrieve wind speed at the primary pixel resolution. Therefore, the numbers of pixels are averaged (to obtain a "cell") to reduce speckles in the S1 data and are then used for retrieval of SSW. Generally, the larger the cell size is, the better its radiometric resolution γ is, which is defined in (2).

In this study, the radiometric resolution is used to describe the speckle "noise" [19].

$$\gamma = 10\log_{10}\left(1 + 1/\sqrt{\mathrm{ENL}}\right) \quad (2)$$

where ENL is the equivalent number of looks, given as:

$$\mathrm{ENL} = \frac{(\mathrm{E[P]})^2}{\mathrm{VAR[P]}} \quad (3)$$

where P is the intensity of pixels obtained from the image, and VAR and E are the variance and mean of P, respectively [20].

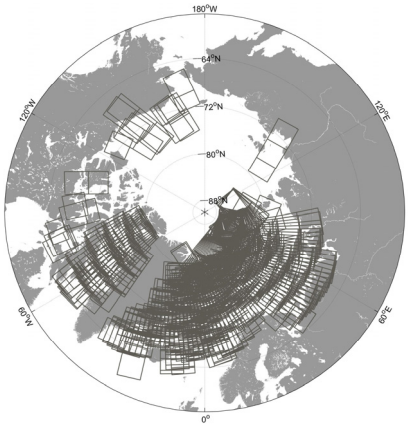

Fig.1. Spatial distribution of the collocations of S1 EW data with the ASCAT measurements from 2015 to 2018.

All 11,431 S1 EW scenes are sampled to different cells with sizes from 200 m to 6 km, and the corresponding derived radiometric resolution (using (2)) is shown in Fig. 2. The radiometric resolution decreases as the cell size increases. However, we also expect to retrieve the SSW from SAR with high spatial resolution (i.e., using a small cell size for retrievals). The absolute calibration accuracy of the S1 data is 0.43 dB [21]. For a cell size of 2 km by 2 km, the mean value of radiometric resolution is 0.37 dB and the standard deviation is 0.08 dB, which is generally lower than the absolute calibration accuracy of the S1 data. Therefore, to balance the trade-off of radiometric resolution and spatial resolution of the retrieved SSW, we chose a cell size of 2 km by 2 km for retrieval.

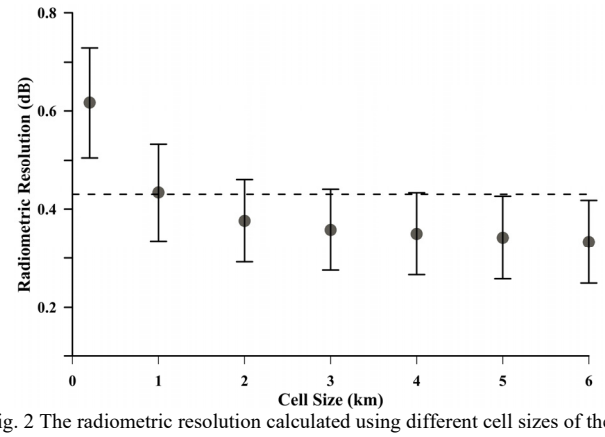

Fig. 2 The radiometric resolution calculated using different cell sizes of the S1 EW data in HH polarization.

As some S1 EW data acquired with a mixture of sea ice and open water, the ice-covered subscenes are filtered out using the ice mapping system (IMS) reanalysis data [22] We checked these data in another study of sea ice detection based on the S1 EW data [23], and they generally show consistency with visual inspection of sea ice cover.

Further, the open water subscenes are screened out using a homogeneity factor, which has been widely applied for

Preprints (www.preprints.org) | NOT PEER-REVIEWED | Posted: 18 May 2020 doi:10.20944/preprints202005.0300.v1

screening SAR data [24] - [26] that contain features making sea surface inhomogeneous, e.g., targets, dark patterns (oil, upwelling, etc.) as well as sea ice. The two steps of preprocessing ensure that the remaining SAR subscenes are suitable for retrieval of SSW. Finally, there are a total of 1,740,509 collocation data pairs were obtained.

B. In situ buoy data

In the present study, 289 scenes of S1 imagery acquired in EW and interferometric wide-swath (IW) modes in HH polarization from October 2014 to October 2019 were collected and matched with data from National Data Buoy Center (NDBC) buoys, yielding a total of 305 data pairs. The ten-minute sea wind measurements of the buoys are used in the following analysis. As the S1 data in VV polarization are generally acquired over buoys, there are not as many data in HH polarization available over the NDBC buoys.

C. Setup and training of the BP neural network

The well-studied GMF presented in (1) suggests that the retrieval of SSW from radar NRCS is a nonlinear relationship. Although the BP neural network is a traditional machine learning algorithm proposed a few decades ago [27], it is a basis of modern neural networks in machine learning and is good at fitting such nonlinear curves.

In the study, the designed BP network consists of an input layer, an output layer and three hidden layers, as illustrated in Fig. 3. The numbers of nodes of the three hidden layers are 6, 10, and 8, respectively. Each neuron connects with all the neurons in the next layer, but there is no connection between neurons in the same layer.

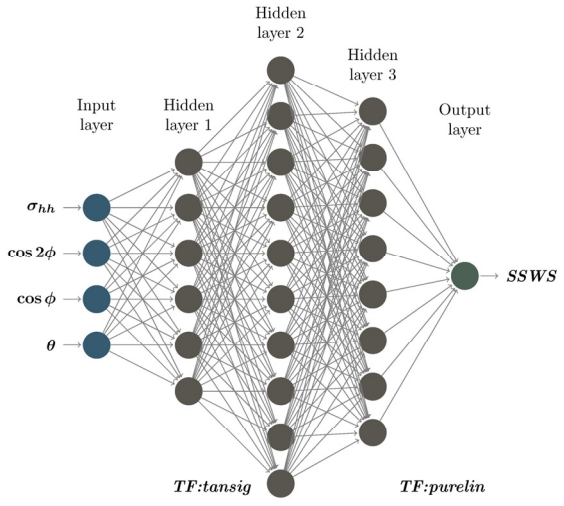

Fig. 3. The structure of the BP neural network developed to retrieve *ssws* from the S1 data.

Based on the expression of the general GMF (referring to (1)), there are four nodes in the input layer of the BP neural network in this study, $\sigma_{\mathrm{HH}}, \cos(\phi), \cos(2\phi)$, and θ.The output layer node of the network has only one value of SSW speed (denoted *ssws* hereafter). The transfer function (abbreviated '*TF*' in Fig.3) of the hidden layer is "*tansig*" (tangent S-type transfer function), which can converge quickly. The output layer transfer function is "*purelin*" (linear transfer function), which can make the network output arbitrary values. The training function is "*traindx*" (momentum BP algorithm with a variable learning rate), which has the fastest convergence speed for a medium-scale BP network. The learning function of the network is "*learngdm*" (gradient descent momentum learning function), which is used to calculate the change rate of weights and thresholds. The performance function of the network is the mean square error (MSE), which is a fast way to measure the "average error".

Because of the difference in the magnitude range of the $\sigma_{\mathrm{HH}}, \cos(\phi), \cos(2\phi)$, and θ values, either the network will not converge or the convergence speed will be very slow. Therefore, before training the network, the input values of $\sigma_{\mathrm{HH}}, \cos(\phi), \cos(2\phi)$, and θ and the output value of *ssws* of the model are normalized, as shown in (4):

$$X_i = \frac{x_i - x_{\min}}{x_{\max} - x_{\min}} \tag{4}$$

where x_i is the input or output data, $x_{\max}$ and $x_{\min}$ are the maximum and minimum values, respectively, of the input or output data, and X_i is the normalized input or output. After normalizing the data, we can train the network using the designed neural network model. Notably, the retrieved $SSWS$ needs to be anti-normalized after training.

Fig. 4 shows the histograms of collocated wind speeds and wind directions. The distribution of collocated wind directions is generally regular over 360 degrees, indicating they can cover various conditions from crosswind to upwind, which yield the lowest and highest radar backscatter of SAR, respectively. However, the distribution of wind speed is close to Rayleigh distribution, in which the cases of high wind speed (e.g., higher than 15 m/s) are greatly reduced. Such an unbalanced training dataset can have a significant impact on the training of the BP network. The training of a BP network ends according to whether the overall bias between the output and the true values is less than a set threshold. Therefore, using less training data with high wind speeds means that such data are taken into account less by the BP network when it tries to fit a nonlinear relationship among $\sigma_{\mathrm{HH}}, \cos(\phi), \cos(2\phi), \theta$ and $ssws$; The majority of the training data are between 2 m/s and 15 m/s.

We used a somewhat "tricky" method to solve this problem. We first randomly chose 80% data of the data with wind speeds lower than 4 m/s, 40% of the data with wind speeds between 4 m/s and 15 m/s, and 80% of the data with wind speeds higher than 15 m/s, which yielded a "pool" of training dataset (822,949 data pairs), denoted $Data_{TR}$. Then, we arbitrarily adjusted these data by duplicating cases in high wind and discarding cases in low to moderate winds, whose histogram roughly fits a normal distribution, as shown by the dark gray bars in Fig. 4(a). They resulted in another training dataset (762,350 data pairs), denoted $Data_{TR\_normal}$.

The training of the neural network is terminated when it meets the requirements of MSE less than 0.001 or training times of 50,000 iterations.

Preprints (www.preprints.org) | NOT PEER-REVIEWED | Posted: 18 May 2020 doi:10.20944/preprints202005.0300.v1

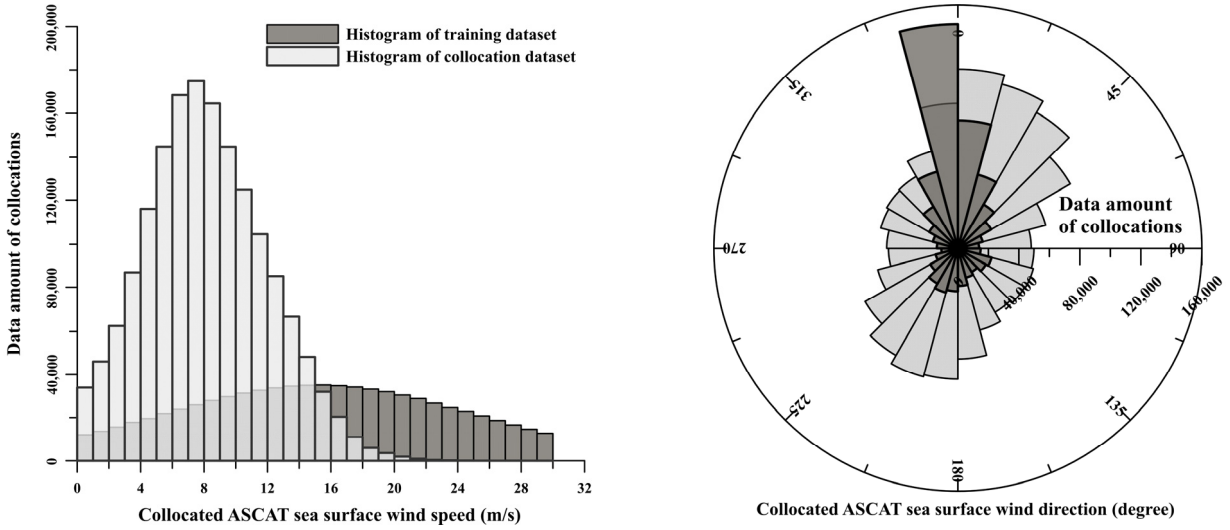

(a) (b)

Fig. 4. Histograms of the S1 SAR collocated sea surface wind speed (a) and wind direction (b). The dark gray bars present the distribution of the data (i.e. the $Data_{TR\_normal}$ described in main text) used for training the BP neural network.

III. Results and Analysis

In this section, we first present verification of the trained network using both the training and testing datasets. Comparisons of the SAR retrieved *ssws* with in situ buoy data and the measurements from the icebreaker "XueLong" during its Arctic surveys in the summer season of 2017 - 2019 are also conducted.

A. Verification of the training BP network for ssws retrieval

Fig. 5 shows the comparisons between the retrieved *ssws* and the collocated ASCAT wind speed based on the training and testing datasets.

Fig. 5 (a): Verification of the training result of the trial using the $Data_{TR}$ directly for training the neural network. The training yields a zero bias. However, the saturation of SAR retrieved $ssws$ at approximately 24 m/s is distinctive, which we have known in the previous studies on SSW retrieval from SAR data on co-polarization using the GMF. Even using all the high wind cases in the collocated data pairs, the saturation problem cannot be solved.

Fig. 5(b): Verification of the training result of another trial using $Data_{TR\_normal}$ for training the neural network. Although the RMSE increases slightly from 1.17 m/s to 1.45 m/s, the S.I. reduces significantly to less than 10%, which is a good indication of data concentration. More importantly, the bias shows very limited dependence on $ssws$, and the saturation does not appear, at least up to the highest $ssws$ of the collocated data pairs, approximately 32 m/s.

Fig. 5(c): Using the same neural network result of (b) but excluding the duplicated cases of the $Data_{TR\_normal}$ from verification. The most distinct change in comparing (c) to (b) is that the bias increases from zero to 0.23 m/s. This is not surprising, as one can see that the amount of data pairs in (c) is only approximately 55% of that in (d), while the training of the neural network seeks an overall minimum bias.

Fig. 5(d): Verification of the neural network result achieved in (b) by using the testing data, which consists of two parts: the collocated data that are not selected for the dataset $Data_{TR}$ and the collocated data that belong to $Data_{TR}$ but not belong to $Data_{TR\_normal}$. Noting that remaining data that are not used for training the neural network are not regular in terms of their wind speed ranges; therefore, the data density in (d) does not change continuously. Comparing the verifications using the testing data and training data (Fig. 5(b)), the bias increases to 0.23 m/s, which indicates that the overall SAR retrievals are higher than the ASCAT wind speeds, whereas the RMSE reduces slightly to 1.25 m/s from 1.41 m/s. On the other hand, the verification using the testing dataset shows the bias in different wind speed ranges remains stable and saturation is not observed.

The trained neural network (Fig. 5(b)) is consequently used to retrieve $ssws$ from the S1 HH-polarized data, and the retrieval is further validated by comparing it with in situ measurements.

B. Comparison of the SAR-retrieved ssws with in situ measurements

The diagram shown in Fig. 6(a) is the comparison of the retrieved $ssws$ based on the BP neural network described above with the NDBC buoy measurements. All the anemometer measurements of wind speed (U_m) at different heights (Z_m) above the sea surface are adjusted to that (U_{10}) at the 10 m height (Z) using (4), assuming conditions of neutral wind [28].

$$\frac{U_{10}}{U_m} = \frac{\ln(Z/Z_0)}{\ln(Z_m/Z_0)} \tag{5}$$

where Z_0 is the roughness length has a value of 1.52×10^{-4}.

The comparison with buoy measurements has a bias of 0.12 m/s and an RMSE of 1.42 m/s. A recent study [29]shows that the retrieval of $ssws$ by S1 HH-polarized data using the CMODH [12] has a bias of 0.49 m/s and an RMSE of 2.05 m/s compared with buoy measurements. This suggests that the proposed machine learning-type retrieval method can also yield accurate estimates of $ssws$ but avoids the complicatedly tuning

Preprints (www.preprints.org) | NOT PEER-REVIEWED | Posted: 18 May 2020 doi:10.20944/preprints202005.0300.v1

of coefficients in the CMOD functions.

Furthermore, we compared the *ssws* retrieved from S1 HH-polarized data with the in situ measurements conducted by the XueLong icebreaker in its three times (2017, 2018, and 2019) surveys in the Arctic. Although only 23 data pairs were collocated, the valuable data are worth of examining. The bias is slightly high of -0.45 m/s, while the RMSE of 1.46 m/s is close to the result achieved in the comparison with NDBC buoy data.

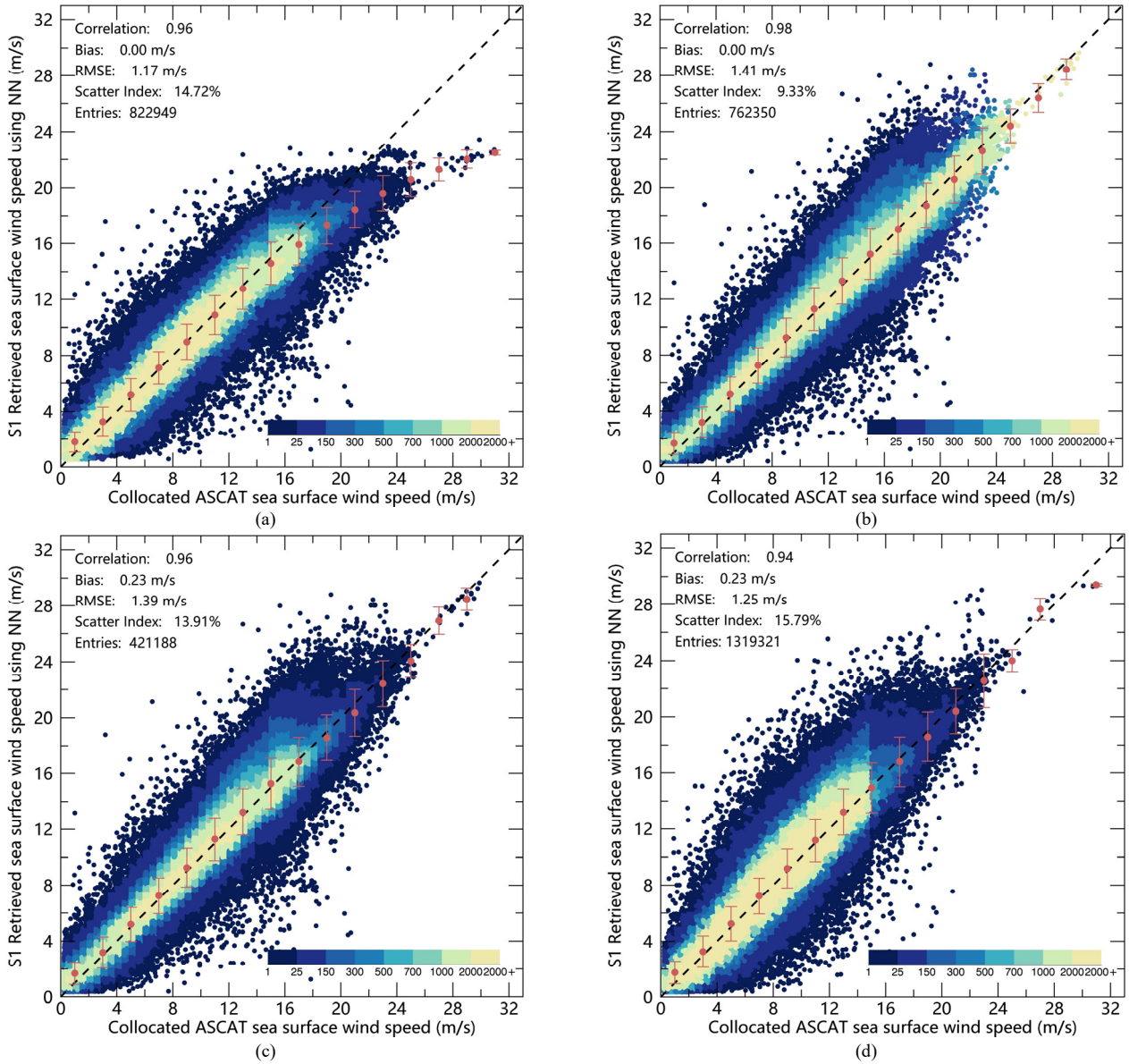

Fig.5 Comparison of the S1-retrieved *ssws* with the collocated ASCAT using different training datasets (a) – (c) and the testing dataset (d). Referring to the main text for detailed explanations.

Preprints (www.preprints.org) | NOT PEER-REVIEWED | Posted: 18 May 2020 doi:10.20944/preprints202005.0300.v1

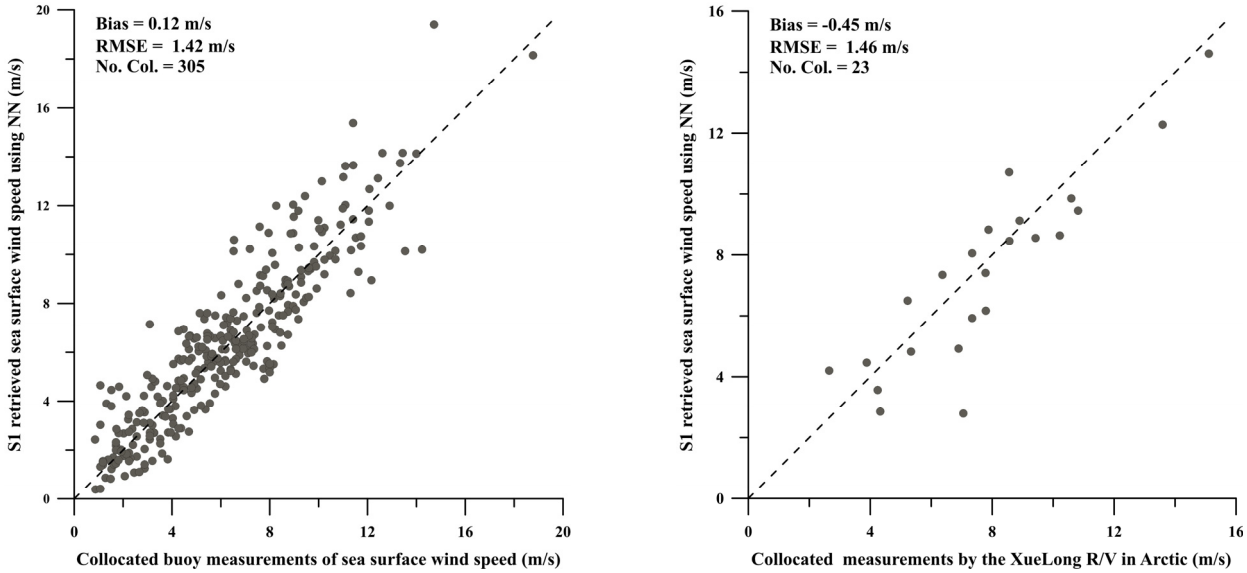

Fig.6 Comparisons of the S1-retrieved *ssws* using the developed BP neural network with the NDBC buoy measurements (a) and with the in situ measurements acquired by the XueLong ice breaker during her Arctic survey (b).

C. Uncertainty of ssws retrieval using the external ERA-5 wind direction

To produce a dataset of S1-derived SSW in the Arctic MIZ, we have to use a reanalysis SSW direction as an external input to the neural network, because it is uniform at both spatial and temporal scales. However, the reanalysis wind data may have biases, which can induce uncertainty in the *ssws* retrieval. The SSW direction of the reanalysis model data is calculated based on its u and v components of the wind field. It is characterized that the ERA-5 has a zonal wind bias of approximately -0.1 m/s and meridional bias of approximately 0.25 m/s in high latitude region of 70°N [30]. As the detailed values of biases are not listed in [30], both numbers are roughly estimated based on Fig. 3 and Fig. 4 in that work. We used the ERA-5 wind direction data (with a grid size of 0.25° and available by each hour) as the input to the trained BP network, and the retrieval is applied to the 11,431 scenes. The results are denoted $ssws_1$. By adding the zonal (u component) and meridional (v component) wind bias of the ERA5 data to the original dataset and applying the same retrieval procedure, we obtained the $ssws_2$.Variations in $\Delta ssws = |ssw_1 - ssw_2|$ with sea surface wind speed and azimuthal wind direction are shown in Fig. 7(a) and (b), respectively.

$\Delta ssws$ shows an overall increasing trend with wind speed. For an *ssws* lower than approximately 19 m/s, the increasing trend is slight, and the mean $\Delta ssws$ is smaller than 0.20 m/s with the maximum standard deviation is of 0.25 m/s. When the *ssws* is high (i.e., higher than 20 m/s), the trend increases rapidly, and the largest mean $\Delta ssws$ reaches 0.38 m/s at a wind speed of 27 m/s. The reason for the decreased $\Delta ssws$ (in terms of both mean and standard deviation values) for a wind speed of 29 m/s is not clear. The number of collocated data in this bin is 4,185, which is comparable to that of neighbor bins, e.g., there are 6,359 and 6,727 in the bins of 25 m/s and 27 m/s, respectively.

The variation in $\Delta ssws$ along with the azimuth wind direction (Fig. 7(b)) shows a periodic fluctuations, following a combination of sine and cosine functions of the azimuth wind angles. Under various wind direction conditions, the $\Delta ssws$ is generally lower than 0.15 m/s.

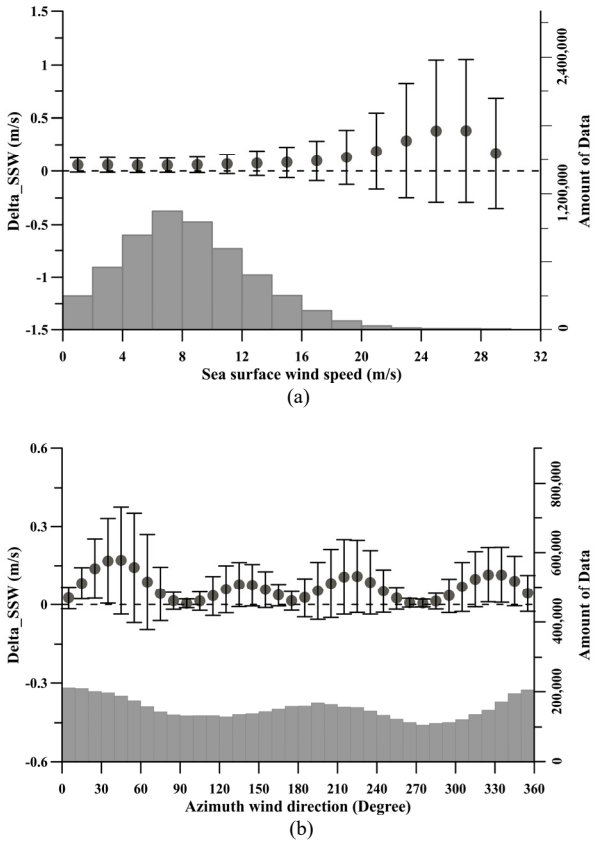

Fig.7 The variations in $\Delta ssws$ along with ERA-5 reanalysis sea surface wind speed and azimuth wind direction.

Preprints (www.preprints.org) | NOT PEER-REVIEWED | Posted: 18 May 2020 doi:10.20944/preprints202005.0300.v1

D. Discrepancy in ssws retrieval from S1A and S1B data

The twins S1A and S1B are identical sensors, but their radiometric calibration accuracy has discrepancies. Both sensors' radiometric calibrations are verified independently. Based on point target measurements, the study in [21] shows that the overall absolute radiometric calibration accuracy of S1A co-polarization data for the Stripmap (SM), IW, and EW modes is of 0.43 dB (1σ). Another study on the independent verification of S1B calibration [31] suggests that the absolute radiometric calibration accuracy of the S1B co-polarization data in EW mode (based on the second and third beams of the five swath beams) is 0.30 dB. This implies that the twin sensors do have some discrepancy in their radiometric calibration, although the difference is only approximately 0.13 dB.

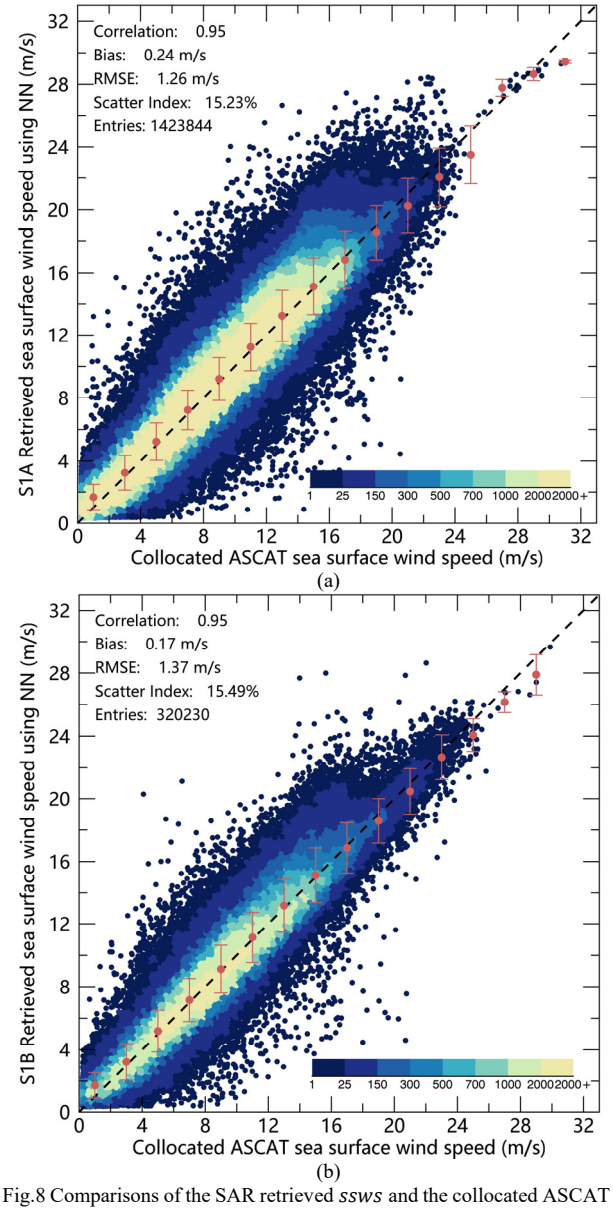

Fig.8 Comparisons of the SAR retrieved *ssws* and the collocated ASCAT wind speed based on the S1A (a) and S1B(b) data.

Fig.8 shows comparisons of the S1A and S1B retrieved *ssws* with the collocated ASCAT wind speed. We did not discriminate between training and testing data in the comparison. The number of the S1A collocations with the ASCAT data is approximately 4 times that of S1B collocations. In fact, the discrepancy between the *ssws* retrievals by the two sensors is almost negligible. The correlation and S.I. of the two comparisons are identical. The bias suggests that the S1B retrieved *ssws* is closer to the ASCAT *ssws* than that from the S1A (0.17 m/s versus 0.24 m/s), while the RMSE values of 1.37 m/s versus 1.26 m/s suggest that the S1A retrievals have better agreement with the ASCAT data than the S1B retrievals.

IV. Discussion

The BP neural network is the basis of a few machine learning models, which is a good candidate for fitting nonlinear relations, making it suitable for deriving some geophysical parameters from satellite data. With respect to retrieving *ssws* by spaceborne SAR data using a neural network, there are generally three sources of uncertainties.

First, there is uncertainty about which inputs are used. For instance, in a previous study [24] the authors used inputs including radar backscatter of SAR alone and both radar backscatter and the collocated scatterometer wind direction. The retrieval results were significantly improved when the wind direction data were used as the input to the neural network (though the expression for inputting the wind direction is unclear). Thanks to long-term investigations on SSW retrieval by scatterometer and SAR, various GMFs have been proposed and the mathematical relationship (which may also be called physical) between radar backscatter and sea surface wind field is clear. Therefore, we decided to use four parameters σ_{HH}, $\cos(\phi)$, $\cos(2\phi)$, and θ as inputs to the network. In our experiments, it was found that the training of the BP neural network rapidly reaches convergency, which can be partially attributed to using appropriate input parameters.

Second, determining the structure of the neural network is a challenge. Although it is well known that the BP neural network has three layers, the difficulty is the design of the number of hidden layers and neurons. We had no better choice than to test various combinations (e.g., the number of hidden layers was increased from 2 to 3, and then to 4) until the retrieval results (output) showed the best agreement with the collocated ASCAT wind speed which was based on the statistical parameters of bias and RMSE. We eventually determined the current structure of the BP neural network for *ssws* retrieval from S1 HH-polarized data. Nevertheless, designing the neural network to achieve the desired goals was difficult.

Last, the distribution of *ssws* is naturally unbalanced, and this problem cannot be fully solved by simply expanding the training dataset. In fact, our collocations of more than 1.7 million are enough to represent various SSW conditions (e.g., as shown in Fig. 4) and we also tried various combinations of data in different wind speed ranges to consist of the training dataset. Once there is a large enough number of training data, the performance of the neural network becomes stable, and the results are generally unchanged even when more training data are added to the network (which may also induce overfitting). In the case of *ssws* retrieval by spaceborne SAR, although the overall bias of zero is very good, it shows a clear dependence on wind speed, i.e., the underestimation trend becomes more

Preprints (www.preprints.org) | NOT PEER-REVIEWED | Posted: 18 May 2020 doi:10.20944/preprints202005.0300.v1

distinct with wind speed increasing. Compared with the fraction of low to moderate wind speed cases of the entire dataset, high wind speed cases (*ssws* larger than 15 m/s) are rare. These rare cases are often neglected by the neural network as "noise", as the training process is terminated based on the overall minimum bias. By duplicating the high wind cases in the training dataset, we arbitrarily enhanced their weights in the neural network. The retrieval results based on both training and testing datasets suggest that this method can partially solve the problem of underestimation of *ssws*.

Although the twins S1A and S1B have some discrepancies in their radiometric calibration, our analysis by comparing their respective retrievals suggests the discrepancy in retrievals is negligible. Since the S1 Instrument Processing Facility (IPF) version 2.90 (available from March 2018; referring to https://qc.sentinel1.eo.esa.int/ipf/), the noise vectors in both the range and azimuth directions have been provided in the EW mode data. Prior to the IPF version 2.90, only the noise vectors in the range direction were available in the EW data. This improvement in noise estimation may lead to a more accurate calibration of the EW mode data. However, we did not treat the EW mode data acquired before and after March 2018 separately in the development of the neural network. We found this improvement (providing noise vectors in the azimuth direction) in the noise estimation has a significant effect on the cross-polarization data in EW mode [32], e.g., by reducing the scalloping effect in the azimuth direction. Nevertheless, along with more S1 EW data are being acquired, one may separate the two sensors' data to develop their respective neural networks and compare the weights and biases of each neuron to figure out the discrepancy in their retrievals of *ssws*.

Thus far, we have used the IMS sea ice cover data to mask the sea ice cover. Notably, that the IMS data are daily available, which is based on multi-sensor observations within one day, while SAR observations are a snapshot. Therefore, the sea ice cover observed by spaceborne SAR has discrepancies with the IMS data, because sea ice drifts. Fig. 9 shows a such case.

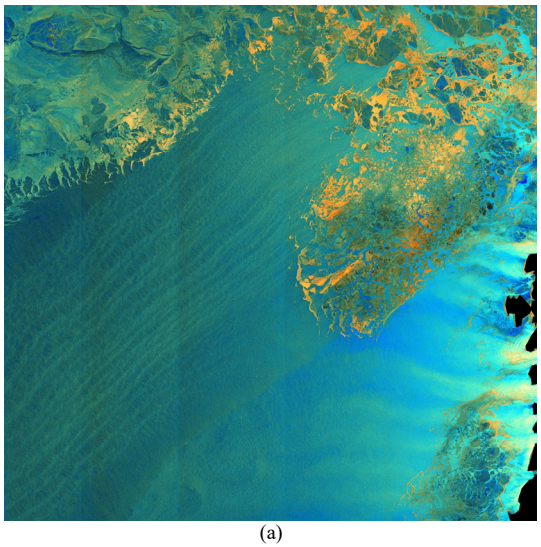

(a)

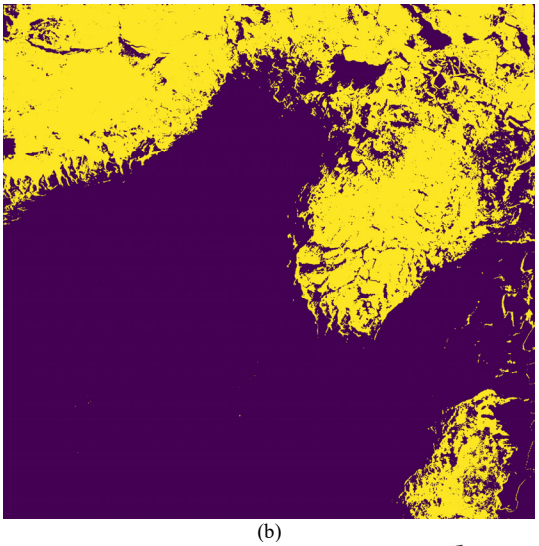

(b)

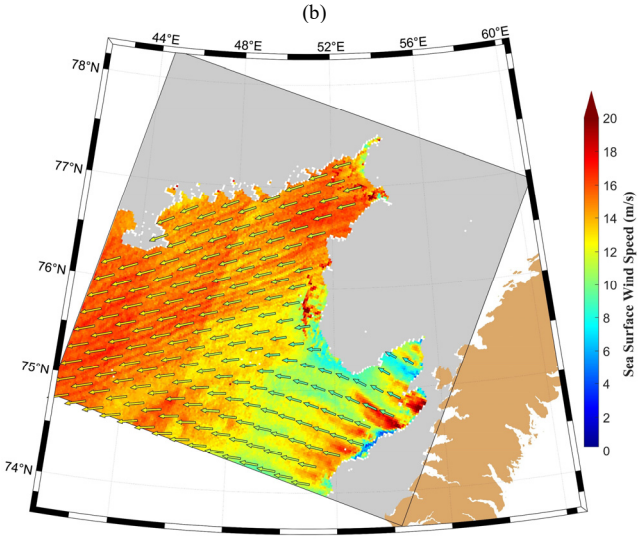

(c)

Fig.9. A case of S1 EW data acquired over the Barents Sea to demonstrate the combination of sea ice cover detection and SSW retrieval. (a) is a false-color composite image based on the HV and HH-polarized images (refer to the main text for details). (b) shows the discrimination of sea ice cover (yellow) and open water (purple) based on the EW data and (c) is the SSW map of the case, where the gray tone represents sea ice cover from the IMS data (note its discrepancy with the result in (b)). The color of the background is the retrieved *ssws* using the developed BP neural network. The ERA-5 reanalysis wind field (colored arrows) in synoptic time is superimposed on the plot for comparison. The ERA-5 wind direction data are used as input to the BP neural network. The Image ID of this case is S1A_EW_GRDM_1SDH_20180404T034739_20180404T034839_021312_024AC5_A80C.

The S1 EW mode data were acquired in April 2018 over the Barents Sea. Fig. 9 (a) shows its false-color composite image based on three channels of HV (red), the difference between HV and HH (green) and the ratio of HV and HH (blue). Note that HV-polarized data of the EW mode over sea ice and open water areas are significantly disturbed by noise, and they should be denoised [32]. Based on the information in the three channels, we developed a deep-learning method (U-net) for discriminating sea ice cover and open water regions, as shown in Fig. 9(b), in which yellow represents sea ice cover with a spatial resolution of 200 m. While the algorithm is being tested

Preprints (www.preprints.org) | NOT PEER-REVIEWED | Posted: 18 May 2020 doi:10.20944/preprints202005.0300.v1

and adjusted for a large dataset of the S1 data acquired in the Arctic to achieve accurate results of sea ice cover, we currently used the IMS data to mask sea ice cover and conduct *ssws* retrieval based on the developed BP neural network, as shown in Fig. 9(c), in which the gray tone represents the sea ice cover from the IMS data. Comparing (c) with (b), one can observe that the IMS sea ice cover is larger than the SAR observation, which is reasonable, as sea ice drifts, and is particularly distinct in the MIZ. If open water areas are marked as sea ice cover, then we lose some information on SSW, as these areas are not used for retrieval. For areas that are sea ice cover as observed by SAR but they are not masked by the IMS (either due to the uncertainty of the IMS data or due to sea ice drifting over time), the following processing step of homogeneity test after sea ice masking can further discard these areas and avoid biased retrieval.

V. Conclusion

With the rapid retreat of sea ice in the Arctic, the MIZ is drawing more attention, as the interaction between sea ice and ocean dynamics is significant and may have feedback affecting seasonal sea ice retreat in the Arctic. Therefore, SSW data with high spatial resolution are highly desirable because of the lack of currently available ice and ocean remote sensing information from space for polar regions.

In this study, we presented a method of retrieving *ssws* from S1 EW data in HH polarization based on a BP neural network. Unlike over other sea areas where most acquisitions of the EW data are in the combination of VV and vertical-horizontal (VH) polarizations, the EW data acquired in the Arctic are combinations of HH and HV polarizations for intensive monitoring of sea ice.

Based on the rather well-developed GMFs for retrieving SSW by spaceborne SAR data, we determined four parameters the radar backscatter σ^0_{HH}, the sea surface wind direction in terms of $\cos(\phi)$ and $\cos(2\phi)$, and the incidence angle θ to use as inputs to the neural network. The structure of the neural network was determined based on various trials. We duplicated the high wind cases in the training dataset to increase their influence on the network performance, which partially solved the problems of underestimating *ssws* for wind speeds above approximately 16 m/s. Comparison of the retrieved *ssws* by the testing dataset (1,319,321 data pairs) with the collocated ASCAT wind speed yields a bias of 0.23 m/s and an RMSE of 1.25 m/s. Although the overall bias suggesting an overestimation than the ASCAT wind speeds, the stepwise comparison (indicated by the error bars in Fig. 5(d)) suggests the bias has a limited dependence on wind speeds. Moreover, the saturation of SSW retrieval generally found in SAR co-polarization data using GMFs is not distinct in the retrievals (up to *ssws* of approximately 30 m/s) using the BP neural network.

We further compared the S1-derived *ssws* with the independent NDBC buoy measurements, in which a bias of 0.12 m/s and an RMSE of 1.42 m/s were obtained. Although data pairs of S1 collocated with the measurements of the XueLong icebreaker acquired in the Arctic surveys are limited, the comparison shows a similar RMSE value to that of the comparison with the NDBC buoy measurements.

As our next step is to produce a sea surface wind field product based on the S1 data acquired in the Arctic since its launch, and we have to use a reanalysis model wind direction data (which has uniform outputs in both space and time) as input to the developed BP neural network, we therefore preliminarily analyzed the effect of the bias of the ERA-5 reanalysis wind model on the retrieval of the S1 *ssws*. Up to 19 m/s of *ssws*, the induced absolute error of retrieval is less than 0.25 m/s. Along with the increase in wind speed, the increasing trend of the absolute error is obvious and can reach 0.38 m/s for the *ssws* of 27 m/s. Interestingly, it is found that the induced absolute error has a periodic variation in azimuthal wind direction, roughly follows a combination of sine and cosine functions.

The discrepancy in respective *ssws* retrieval by S1A and S1B is almost negligible, which may be partially because that their collocations with ASCAT were combined in training the BP neural network. A separate training can probably avoid differing performance in the *ssws* retrievals due to their discrepancy in radiometric calibration accuracy. Along with developing a robust method of discriminating sea ice and open water from S1 EW data, we will combine this method with SSW retrievals to obtain synergistic information on sea ice and ocean dynamic parameters in the MIZ of the Arctic.

Appendix

In the following, the processing steps for retrieving *ssws* from the S1 EW data using the developed BP neural network are provided. The MATLAB functions used are written in ***bold and italic***.

Step 1: Reading the S1 data and conducting radiometric calibration

The digital number (DN) values ($\mathrm{DN_i}$) of the S1 data are read from the Geotiff data and the calibration vector ($\mathrm{A_i}$), noise vector (η_i), latitude matrix (lat), longitude matrix (lon), incidence angle matrix (inc) and look angle (look_angle) are read from the annotation files (.XML).

The S1 data are radiometrically calibrated using the following equation:

$$\sigma^0_{HH}(\mathrm{i}) = \frac{\mathrm{DN_i^2} - \eta_\mathrm{i}}{\mathrm{A_i^2}}. \qquad \text{(A1)}$$

At the same time, the matrices of σ^0_{HH}, lat, lon and inc are interpolated to grids, where each grid has a size of 2 km by 2 km.

Step 2: Masking and homogeneity test

We use the Global Self-consistent, Hierarchical, High-resolution Geography Database (GSHHG) coastal line data [33] to mask the land area in the S1 images. Then, the IMS data are used to mask the sea ice cover. As mentioned in the main text, there are discrepancies in sea ice cover between SAR observations and IMS data. On the other hand, there may exist other features that disturb the sea surface and make the data unsuitable for SSW retrieval, we use the homogeneity factor [25] to exclude these grids from retrievals. The factor is defined as:

Preprints (www.preprints.org) | NOT PEER-REVIEWED | Posted: 18 May 2020 doi:10.20944/preprints202005.0300.v1

$$\xi_H = \left(\sum_k \overline{\text{mean}}(\hat{\Phi}_k)\right)^{-1} \sum_k \frac{\overline{\text{var}}(\hat{\Phi}_k)}{\overline{\text{mean}}(\hat{\Phi}_k)} \quad \text{(A2)}$$

And

$$\overline{\text{var}}(\hat{\Phi}_k) = \frac{1}{N}\sum_{j=1}^{N}(\hat{\Phi}_k^j)^2 - \text{mean}(\hat{\Phi}_k)^2 \quad \text{(A3)}$$

We further divide each SAR subimage (2 km × 2 km) into 2×2 subgrids to calculate the homogeneity factor, i.e. $N = 2$ in (A2) and (A3). The image power spectrum $\hat{\Phi}_k$ of each subgrid is estimated by FFT. The S1 subimage with a homogeneity factor ≤ 1.05 is used for $ssws$ retrieval. However, as this threshold is determined based on empirical experience (visual inspections), we have found that some retrievals are acceptable when their homogeneity factors are between 1.05 and 1.50. Therefore, the $ssws$ retrievals from the sub-images which have the homogeneity factor in this range ([1.05, 1.5]) are defined as "suspecting" results in the NetCDF product.

Step 3: Matching S1 data with the ERA-5 reanalysis wind model data

Following the preprocessing in the above two steps, each S1 subimage is temporally and spatially matched with the ERA-5 reanalysis wind data.

As the ERA-5 reanalysis wind model data is available each hour, the temporal difference between the S1 observation and the model is no larger than 30 minutes. With respect to temporal collocation, the u and v components of the ERA-5 wind data at the four (model) grids nearest to the S1 subimage are bilinearly interpolated to the location of the subimage. Based on the u and v components, one can derive wind direction and the consequent azimuthal wind direction ϕ by taking into account the SAR looking angle.

After matching the S1 observations with the ERA-5 reanalysis wind data, each S1 subimage has four inputs available, i.e. σ^0_{HH}, θ, $\cos(\phi)$ and $\cos(2\phi)$ for the trained BP neural network, which compose an array in MATLAB:

$$Array_{input} = [\sigma^0_{HH} \;\; \cos(\phi) \;\; \cos(2\phi) \;\; \theta]$$

Step 4: Retrieval of $ssws$ using the BP neural network

We applied the MATLAB function ***mapminmax*** to scale the input to the range $[-1,1]$:

$$Array_{input\_norm} = mapminmax(Array_{input}) \quad \text{(A4)}$$

Then, we applied the MATLAB function ***sim*** to retrieve the $ssws$:

$$ssws_{norm} = sim(BP_{net}, array_{input_{norm}}) \quad \text{(A5)}$$

The output of the neural network $ssws_{norm}$ is a normalized retrieved sea surface wind speed and needs to be anti-normalized to obtain the true wind speed. We set the min and max values of normalizing the sea surface wind speed to be 0 and 30. Note that setting of the maximum value of 30 m/s to normalize $ssws$ does not limit the retrievals cannot be over 30 m/s as the network can output values of $ssws_{norm}$ larger than 1.0.

The weights and biases of the trained BP neural network are stored in the matrix BP_{net}, which are provided in the Table A1.

REFERENCES

[1] A. Stoffelen and D. Anderson, "Scatterometer data interpretation: Estimation and validation of the transfer function CMOD4," *J. Geophys. Res*., vol. 102, no. C3, pp. 5767-5780, Mar. 1997, DOI: 10.1029/96JC02860.

[2] H. Hersbach, A. Stoffelen, and S. de Haan, "An improved C-band scatterometer ocean geophysical model function: CMOD5," *J. Geophys. Res*., vol. 112, no. C3, pp. 4018-4073, Mar. 2007, DOI: 10.1029/2006JC003743.

[3] H. Hersbach, "Comparison of C-band scatterometer CMOD5.N equivalent neutral winds with ECMWF," *J. Atmos. Oceanic Technol.*, vol. 27, no. 4, pp. 721-736, Apr. 2010.

[4] A. Elyouncha, X. Neyt, A. Stoffelen, and J. Verspeek, "Assessment of the corrected CMOD6 GMF using scatterometer data," *in Proc. Remote Sensing of the Ocean, Sea Ice, Coastal Waters, and Large Water Regions*, Toulouse, France, Sep. 2015, vol. 9638.

[5] A. Stoffelen, J. A. Verspeek, J. Vogelzang, and A. Verhoef, "The CMOD7 geophysical model function for ASCAT and ERS wind retrievals," *IEEE J. Sel. Topics Appl. Earth Observ. Remote Sens*., vol. 10, no. 5, pp. 2123-2134, May. 2017, DOI: 10.1109/JSTARS.2017.2681806.

[6] Y. Quilfen, B. Chapron, T. Elfouhaily, K. Katsaros, and J. Tournadre, "Observation of tropical cyclones by high-resolution scatterometry," *J. Geophys. Res*., vol. 103, no. C4, pp. 7767-7786, Apr.1998, DOI: 10.1029/97JC01911.

[7] T. Elfouhaily, D. R. Thompson, and D. Vandemark, "A new biostatic model for electromagnetic scattering from perfectly conducting random surfaces," *Waves in Random Media*, vol. 9, no. 3, pp. 281-294, 1996.

[8] A. A. Mouche, D. Hauser, J. F. Daloze, and C. Guerin, "Dual-polarization measurements at C-band over the ocean: results from airborne radar observations and comparison with ENVISAT ASAR data," *IEEE Trans. Geosci. Remote Sens.*, vol. 43, no. 4, pp. 753-769, Apr. 2005, DOI: 10.1109/TGRS.2005.843951.

[9] G. H. Liu, X. F. Yang, X. F. Li, B. Zhang, W. Pichel, Z. W. Li, and X. Zhou, "A systematic comparison of the effect of polarization ratio models on sea surface wind retrieval from C-band synthetic aperture radar," *IEEE J. Sel. Topics Appl. Earth Observ. Remote Sens*., vol. 6, no. 3, pp. 1100-1108, Jun. 2013, DOI: 10.1109/JSTARS.2013.2242848.

[10] B. Zhang, W. Perrie, and Y. J. He, "Wind speed retrieval from RADARSAT-2 quad-polarization images using a new polarization ratio model," *J. Geophys. Res*., vol. 116, no. C8, Aug. 2011, DOI: 10.1029/2010JC006522.

[11] F. M. Monaldo, D. R. Thompson, W. G. Pichel, and P. Clemente-Colon, "A systematic comparison of QuikSCAT and SAR ocean surface wind speeds," *IEEE Trans. Geosci. Remote Sens.*, vol. 42, no. 2, pp. 283-291, Feb. 2004, DOI: 10.1109/TGRS.2003.817213.

[12] B. Zhang, A. Mouchee, Y. Lu, W. Perriee, G. S. Zhang, and H. Wang, "A geophysical model function for wind speed retrieval from C-band HH-polarized synthetic aperture radar," *IEEE Geosci. Remote Sens. Lett.*, vol. 16, no. 10, pp. 1521-1525, Oct. 2019, DOI: 10.1109/LGRS.2019.2905578.

[13] O. Isoguchi and M. Shimada, "An L-band ocean geophysical model function derived from PALSAR," *IEEE Trans. Geosci. Remote Sens.*, vol. 47, no. 7, pp. 1925-1936, Jul. 2009, DOI: 10.1109/TGRS.2008.2010864.

[14] X. M. Li and S. Lehner, "Algorithm for sea surface wind retrieval from TerraSAR-X and TanDEM-X data," *IEEE Trans. Geosci. Remote Sens.*, vol. 52, no. 5, pp. 2928-2939, May. 2014, DOI: 10.1109/TGRS.2013.2267780.

[15] C. Strong and I. G. Rigor, "Arctic marginal ice zone trending wider in summer and narrower in winter," *Geophys Res. Lett.*, vol. 40, no. 18, pp. 4864-4868, Sep. 2013, DOI: 10.1002/grl.50928.

[16] T.T. Qin, X.M. Li, T. Jia, and Q. Feng, "Retrieval of ocean surface wind speed using Sentinel-1 HH polarization data," *2019 SAR in Big Data Era (BIGSARDATA)*, Beijing, China, 2019, pp. 1-4.

[17] X. F. Li, B. Liu, G. Zheng, Y. B. Ren, S. S. Zhang, Y. J. Liu, L. Gao, Y. H. Liu, B. Zhang, and F. Wang, "Deep learning-based information mining from ocean remote sensing imagery," *Nati. Sci. Rev.*, Mar. 2020, [Online]. Available: https://doi.org/10.1093/nsr/nwaa047

[18] ESA (European Space Agency), "Sentinel-1 product specification," 2016. [Online]. Available: https://sentinel.esa.int/web/sentinel/document-library/content/-/article/sentinel-1-product-specification

[19] P. Olivier and D. Vidal-Madjar, "Empirical estimation of the ERS-1 SAR radiometric resolution," *Int. J. Remote Sens.* , vol. 15, no. 5, pp. 1109-1114, Mar.1994, DOI: 10.1080/01431169408954144.

[20] A Moreira, "Improved multi-look techniques applied to SAR and SCANSAR imagery," *IEEE Trans. Geosci. Remote Sens.*, vol. 29, no. 4, pp. 529-534, Jul. 1991, DOI: 10.1109/36.135814.

[21] M. Schwerdt, K. Schmidt, N. T. Ramon, G. C. Alfonzo, B. J. Doring, M. Zink, and P. Prats-Iraola, "Independent verification of the Sentinel-1A system calibration," *IEEE J. Sel. Topics Appl. Earth Observ. Remote Sens.,* vol. 9, no. 3, pp. 994–1007, Mar. 2016, DOI: 10.1109/JSTARS.2015.2449239

[22] S. R. Helfrich, D. McNamara, B. H. Ramsay, T. Baldwin, and T. Kasheta, "Enhancements to and forthcoming developments in the Interactive Multisensor Snow and Ice Mapping System (IMS)," Hydrol. Process., vol. 21, no. 12, pp. 1576-1586, Jun. 2007.

[23] X. M. Li, Y. Sun, and Q. Zhang, "Extraction of sea ice cover by Sentinel-1 SAR based on SVM with unsupervised generation of training data," *IEEE Trans. Geosci. Remote Sens.*, under revision, 2020.

[24] J. Horstmann, H. Schiller, J. Schulz-Stellenfleth, and S. Lehner, "Global wind speed retrieval from SAR," *IEEE Trans. Geosci. Remote Sens.*, vol. 41, no. 10, pp. 2277-2286, Oct. 2003, DOI: 10.1109/TGRS.2003.814658.

[25] J. Schulz-Stellenfleth and S. Lehner, "Measurement of 2-D sea surface elevation fields using complex synthetic aperture radar data," *IEEE Trans. Geosci. Remote Sens.*, vol. 42, no. 6, pp. 1149-1160, Jun. 2004, DOI: 10.1109/TGRS.2004.826811.

[26] X. M. Li, S. Lehner, and T. Bruns, "Ocean wave integral parameter measurements using Envisat ASAR wave mode data," *IEEE Trans. Geosci. Remote Sens.*, vol. 49, no. 1, pp. 155-174, Jun. 2011, DOI: 10.1109/TGRS.2010.2052364.

[27] D. Rumelhart, G. Hinton, and R. Williams, "Learning representations by back-propagating errors," *Nature,* vol. 323, no. 6088, pp. 533–536, Oct. 1986, DOI: 10.1038/323533a0.

[28] J. P. Peixoto and A. H. Oort, "Physics of climate," *American Institute of Physics*, vol. 45, no. 8, pp. 67-67, 1992.

[29] Y. R. Lu, B. Zhang, W. Perrie, A. Mouche, and G. S. Zhang, "CMODH validation for C-band synthetic aperture radar HH polarization wind retrieval over the ocean," *IEEE Geosci. Remote Sens. Lett.*, vol. 99, no. 10, pp. 1-5, Jan. 2020, DOI: 10.1109/LGRS.2020.2967811.

[30] M. B. Rivas and A. D. Stoffelen, "Characterizing ERA-Interim and ERA-5 surface wind biases using ASCAT," *Ocean Sci.*, vol. 15, no. 3, pp. 831–852, Jan. 2019.

[31] M. Schwerdt, K. Schmidt, N. T. Ramon, P. Klenk, N. Yague-Martinez, P. Prats-Iraola, M. Zink, and D. Geudtner, "Independent system calibration of Sentinel-1B," *Remote Sens.*, vol. 9, no. 6, Jun. 2017, DOI: 10.3390/rs9060511.

[32] Y. Sun and X. M. Li, "Denoising Sentinel-1 extra-wide mode cross-polarization images over sea ice," *IEEE Trans. Geosci. Remote Sens.*, under revision, 2020.

[33] P. Wessel and W. H. F. Smith, "A global self-consistent, hierarchical, high-resolution shoreline database," *J. Geophys. Res.*, vol. 101, no. B4, pp. 8741-8743, Apr. 1996, DOI: 10.1029/96JB00104.

ACKNOWLEDGMENT

The S1 SAR data are downloaded from the Copernicus data hub (https://scihub.copernicus.eu/), and the ASCAT data are accessed from EUMETSAT. Use of the reference data of ERA-5 (https://cds.climate.copernicus.eu/cdsapp#!/home), IMS data (https://www.natice.noaa.gov/ims/) and GSHHG data (https://www.soest.hawaii.edu/pwessel/gshhg/) is also acknowledged.

Preprints (www.preprints.org) | NOT PEER-REVIEWED | Posted: 18 May 2020 doi:10.20944/preprints202005.0300.v1

TABLE A1

THE WEIGHTS OF NEURONS CONNECTING THE INPUT LAYER (ROW) AND THE FIRST HIDDEN LAYER (COLUMN)

	Neuron 1	…	…	Neuron 4
Neuron 1	1.35799401462446	-1.10259316914732	0.335981355623764	0.272512797610827
…	-2.36441248024990	1.03503460476278	0.543268223117868	-1.49702712335111
…	-2.28049553757969	-0.464650444976570	0.317823811389357	-1.21443905897947
…	-2.21693910117561	0.0383351731986321	0.282252861921783	-0.0613427064770843
…	-0.270660648829750	1.41445838668801	0.668843417713446	0.496561569414443
Neuron 6	-1.60231069909676	-0.195465009443951	0.728880985579777	-1.10445019344022

THE WEIGHTS OF NEURONS CONNECTING THE FIRST HIDDEN LAYER (ROW) AND THE SECOND HIDDEN LAYER (COLUMN)

	Neuron 1	…	…	…	…	Neuron 6
Neuron 1	1.1397920256150	1.89661266986153	-1.283773847885	0.085187536483929	-0.063459295262	-1.162136873516
…	-0.198358601266	1.36394018568907	1.57253186821047	-1.148018805309	0.231112562654413	0.645796503500879
…	-0.678142348763	-0.199461939342	1.01869958730975	1.46781374438703	-0.041822043747	-0.712885953434
…	0.1910453831996	1.14768330387281	0.498706446019045	0.452359997020326	1.19089307746359	-1.355978406219
…	0.3849750801359	-1.177105608704	1.54472685609111	0.632812104673446	0.100762037819503	0.704017088900113
…	0.5032146711624	-0.899832114283	1.03126116077854	-0.687996417608	0.578206049832177	0.009656430341968
…	1.0820875254610	0.627483501361421	1.97723402406411	0.885647029665893	-0.532557259337	-0.639919305010
…	0.5979511985770	1.24509069053319	0.415655062240200	-0.489321038622	0.912386007906291	-1.036934496026
…	0.6169216114075	-0.588978212579	2.32443511996747	-0.338686199388	-0.752987408030	-0.453853733339
Neuron 10	0.3488855414082	0.000244118790022	0.700448757317926	-2.273538016844	0.201986903576005	0.869807053825020

THE WEIGHTS OF NEURONS CONNECTING THE SECOND HIDDEN LAYER (ROW) AND THE THIRD HIDDEN LAYER (COLUMN)

	Neuron 1	…	…	…	…	…	…	…	…	Neuron 10
Neuron 1	1.0387134	-1.286728	-0.392615	-0.918542	0.2233739	-0.324166	-0.166188	0.4237303	1.0779886	0.7406658
	6707379	76290900	921447484	209953449	33854063	732629374	842209020	02842222	7366136	35665252
…	-1.006663	0.0788090	-0.034908	-1.281439	-0.658215	-0.770763	0.0736626	0.1961303	-0.242265	1.1262639
	78061236	379982044	183036705	44528808	248375978	163056224	773265441	52054691	264811827	6208120
…	0.3520905	-1.105574	-0.393935	-1.407932	1.1447989	0.2425887	-2.848675	0.7604654	-1.045264	1.8286696
	41064823	73139957	445745547	33049740	7459074	48827192	53200052	95635649	00804428	3454512
…	-1.251848	-0.002921	0.7935489	-0.413759	-0.386891	0.1837802	0.6056033	-0.445297	-0.558112	0.2419876
	34604807	328603112	42102038	943228806	235719630	50647745	88328891	473437239	568469832	49922061
…	-1.005888	-1.275323	0.3562453	-0.255098	0.2359288	-0.120358	-0.973247	-0.677960	-0.347725	-1.003807
	44808547	39992951	60443631	835380100	47743238	788060656	795963073	006377093	829272019	01043712
…	-1.482462	1.6969135	-0.045767	-1.034607	-0.897943	-0.533440	0.4041267	0.0337563	-0.026170	-0.510112
	74565115	7574192	538939816	07870829	172841501	548692554	14539928	000929784	987394873	218260637
…	-1.444093	-0.036753	-0.036414	-0.602262	0.1857092	0.5960770	-0.741236	-0.033596	1.4159200	0.2496935
	74386379	118357037	262633473	857817669	87142008	15455694	406603249	430450842	4992181	39119471
Neuron 8	-0.656092	-0.731203	0.1285923	0.4586477	1.4556264	-0.465070	-0.225582	0.4680555	0.7984297	0.6877344
	230151342	026026613	07275371	46149548	7650427	471822353	844718152	22497490	73320449	03258738

THE WEIGHTS OF NEURONS CONNECTING THE THIRD HIDDEN LAYER (ROW) AND THE OUTPUT LAYER (COLUMN)

	Neuron 1	…	…	…	…	…	…	Neuron 8
Neuron 1	0.4029406987	1.0722908532	1.8064761705	-0.514197995	0.3036328792	-0.974434882	0.7779415527	-1.026315289

THE BIAS OF NEURONS IN THE FIRST HIDDEN LAYER

Neuron 1	…	…	…	…	Neuron 6
-2.20530861321237	1.70505319262913	1.40897518132112	1.53185999556214	-0.892858805540525	-1.28878524037813

THE BIAS OF NEURONS IN THE SECOND HIDDEN LAYER

Neuron 1	…	…	…	…	…	…	…	…	Neuron 10
-1.6383213	-1.5810461	0.78122489	-0.6796223	0.15719104	0.70699193	0.50946988	1.40529511	1.80579509	2.31071207
9090154	7255786	0952619	20647683	5400725	8763485	4095470	309813	259162	212034

THE BIAS OF NEURONS IN THE THIRD HIDDEN LAYER

Neuron 1	…	…	…	…	…	…	Neuron 8
-1.53076034415	1.308441784515	-1.06924300491	0.225317438845	-0.14620232293	-0.72731241228	-0.75848764460	-2.05859481314
164	66	170	222	6459	6867	7696	414

THE BIAS OF NEURONS IN THE OUTPUT LAYER

Neuron 1
0.577119828493821